

HSI Shadow Enhancement Based on D-DSR and Classification with Parameter Optimization

Yangyang Kou, Xuefeng Liu

Abstract—Hyperspectral image (HSI) has been widely applied in many fields because of its rich ground target information. Classification is one of the effective means to explore the information in HSIs. However, some HSIs contain shadow areas due to lighting, occlusion and other reasons, usually treated as a separate category or discarded directly. Most image enhancement methods remove the noise in the shadow regions with the loss of many valuable signals. Dynamic stochastic resonance (DSR) can enhance the signal by using noise to generate resonance. Therefore, a double dynamic stochastic resonance (D-DSR) method of shadow enhancement is proposed in this paper by twice successive DSRs in the spatial dimension of HSI. Meanwhile, a parameter-optimized convolution neural network (CNN) model is presented and applied to HSI classification. Firstly, through the horizontal and vertical sampling in two different spatial directions, the shadow area can be enhanced by D-DSR while maintaining the consistency of the enhancement degree of the horizontal and vertical textures. Secondly, the enhanced HSI can be obtained by fusing the shadow area processed by D-DSR with the original image. Thirdly, with parameter optimization, CNN can be used to classify the enhanced HSI. Finally, to evaluate the performance of the proposed method, the comparative experiments are conducted on a real-world HSI. The experimental results show that the proposed approach can help improve the classification and has potential prospects in HSI processing.

Index Terms—Double dynamic stochastic resonance, remote sensing image, shadow enhancement, classification.

I. INTRODUCTION

HYPERSPECTRAL image (HSI) provide rich scene information that can reveal details about each location in the two-dimensional space and multiple characteristics from different spectral bands [1]. As hyperspectral imaging technology continues to mature, HSI is playing a significant role in various fields such as space exploration, weather forecasting, environmental monitoring, medical diagnosis, and industrial quality inspection [2-5].

Classification is a highly effective method of analysis extensively used for processing HSI. Traditional classification methods include support vector machine (SVM) [6] and principal component analysis (PCA). However, in recent years,

convolutional neural network (CNN) has been introduced for hyperspectral image classification, and it has achieved better results than traditional classifiers due to its stronger feature extraction and learning capabilities.

Some HSIs contain shadow regions that occur due to light obscuration, clouds, ground undulations, or ground objects [7]. The intense noise and weak signal in these shadow regions make data processing extremely challenging [8]. Most of the current image enhancement and pixel classification methods focus on removing or processing shadows, leading to a loss of vital information in the shadow region [9]. It is necessary to enhance the shadow region information for subsequent HSI classification, which can greatly improve the efficiency of human-computer interaction and the performance of computer vision techniques such as target detection [10], classification [11,12], and tracking [13].

Stochastic resonance (SR) theory, which applies to amplify weak signals in intense noise environments, has been utilized for enhancing shadow information in HSIs [14]. In a bistable nonlinear system, noise can be used to generate resonance and convert its energy to the signal so that the signal can be enhanced. This lays the foundation for the extraction of shadow information in HSIs.

Liu et al. [15] proposed a grayscale image restoration enhancement method based on adaptive bistatic array SR in a low peak signal-to-noise ratio environment, while Chouhan et al. [16] presented a dynamic stochastic resonance (DSR)-based spatial domain analysis method to enhance low-contrast images. However, these methods have limitations when applied to HSI due to non-uniform illumination.

This paper introduces the double dynamic stochastic resonance (D-DSR) algorithm, which is based on a bistable nonlinear system and consists of two consecutive DSRs. DSR can only perform texture enhancement in a certain gradient in either the horizontal or vertical direction, resulting in a lack of texture enhancement in the other direction. By enhancing in two different directions, D-DSR preserves the correlation between adjacent pixels in HSI and maintains the consistency of horizontal and vertical texture enhancement to a greater extent than DSR. Consequently, the enhanced images retain more of the original information and have a more significant shadow area enhancement.

Since the results of HSI classification depend on both spatial and spectral information, a three-dimensional convolutional neural network (3D-CNN) can extract both types of information simultaneously and achieve high classification accuracy. However, the optimal parameters of 3D-CNN for different HSIs vary. If empirical or default values are selected, overfitting, considerable convergence time, or some

Manuscript received January 4, 2023; revised June 26, 2023.

This work was supported in part by the National Natural Science Foundation of China under Grant 61971253 and the Shandong Provincial Natural Science Foundation ZR2020MF011.

Y.Y. Kou is a postgraduate student at the School of automation and Electronic Engineering, Qingdao University of Science and Technology, Qingdao 266061, China. (e-mail: 2021040011@mails.qust.edu.cn).

X.F. Liu is a professor at the School of automation and Electronic Engineering, Qingdao University of Science and Technology/ Shandong Key Laboratory of Autonomous Landing for Deep Space Exploration, Qingdao 266061, China. (Corresponding author to provide e-mail: nina.xf.liu@hotmail.com).

output error may occur, making it difficult to converge to the global or local optimum. Therefore, this paper considers parameter optimization to improve training efficiency and minimize network error, making the 3D-CNN model suitable for real-world HSI.

To evaluate the proposed D-DSR method's performance, the paper conducts comparison experiments on a real-world dataset using different denoising algorithms. The results show that the D-DSR algorithm outperforms other algorithms in improving the classification accuracy of HSI shadow regions.

Section 2 briefly introduces SR theory, DSR method, and 3D-CNN algorithm. The proposed D-DSR denoising method is presented in Section 3.1, and the paper explains the parameter optimization of the classification model in Section 3.2. Section 4 presents the comparative experiments on the proposed approach, and Section 5 analyzes and discusses the experimental results. Finally, Section 6 concludes the paper.

II. RELATED WORKS

A. Overview of SR

Italian physicist Milutin Milankovitch was the first to explain the glacial phenomenon that occurred every 100,000 years during the earth's ancient past, but it was the Italian physicist, Benz, who named it the SR theory. This phenomenon is caused by the synchronization of the cycle of weak radiation exerted by the sun on the earth with the process of glacial turnover in a nonlinear environment. The environment is disrupted by short-term climate changes on earth. Nowadays, SR theory has been widely applied to the amplification of weak signals in a strong noise environment. In such cases, noise energy can be converted into signal energy when the nonlinear system, noise, and weak signal are in concert. In HSI, the shaded region can be regarded as intense noise, and therefore, SR lays the foundation for information extraction from the shady part of the HSI. SR theory has been successfully applied in image enhancement.

Ye et al. [17] enhanced the image's direct current component using a bistable system, and Marks et al. [18] found that the appropriate intensity of noise added to the image could make it more consistent with human visual features. Leng et al. [19] used a comparable specialization of SR to stretch a given histogram distribution of a noisy image and obtained an enhanced image by adjusting the parameters of the resonant system. They demonstrated the effect of a bistable double SR system on the histogram. DSR [14], which is a derivative approach of SR, has also been an effective shadow enhancement method.

The bistatic model-based SR falls under the traditional SR, which adheres to the classical SR theory consisting of three necessary conditions: a weak signal, noise, and a nonlinear system. Macroscopically, the bistable nonlinear system can be seen as the motion of a small ball in a bistable potential well under the over-damping condition, as illustrated in Figure 1. The dual potential wells in the figure represent the two valleys. The system's kinetic equation is expressed by Equation (1) [21]:

$$\frac{dx(t)}{dt} = -\frac{\partial U(x)}{\partial x} + f(t) + \xi(t) \quad (1)$$

here, t represents time, $\frac{dx(t)}{dt}$ is the rate of change of the globule position, $f(t)$ is the external periodic signal input, $\xi(t)$ is the noise, and $U(x)$ is the potential function. In the SR theory, $U(x)$ is commonly expressed as a bistable fourth-order potential well function, which is represented by the following equation (2) [22]:

$$U(x) = -a\frac{x^2}{2} + b\frac{x^4}{4} \quad (2)$$

where a and b represent the two parameters of the system, and both must be greater than 0. As the HSI's pixel values are non-negative, the SR process can only be performed in the positive potential well. Therefore, this paper only considers the single-well characteristic, specifically the proper potential well.

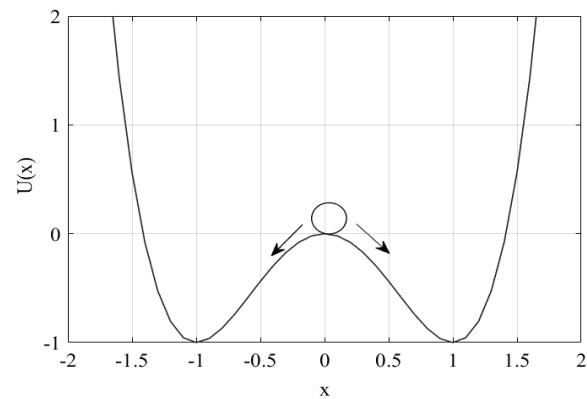


Fig. 1. Bistable non-linear system potential function represented by $U(x)$ ($a=4$, $b=4$).

To obtain the Langevin equation, equation (2) is substituted into equation (1) and then simplified. The resulting expression is shown in equation (3). The Langevin equation describes the motion of a particle under superdamping and can be solved using the fourth-order Runge-Kutta method.

$$\frac{dx}{dt} = ax - bx^3 + f(t) + \xi(t) \quad (3)$$

The three states of the sphere are illustrated in Figure 1: $x = \pm\sqrt{\frac{a}{b}}$ in the steady state, and $x=0$ in the unsteady state. The values of a and b determine the position of x in these three states, as well as the height of the potential barrier of the system, which is $\Delta U = \frac{a^2}{4b}$. When the noise is zero, the system exhibits periodic motion in the vicinity of $x = \pm\sqrt{\frac{a}{b}}$, provided the leap's critical value is not reached. In the presence of noise, however, the system can shift the signal from weak to strong, making a large jump motion in the potential well, even if the system does not reach the critical value. By continuously adjusting the noise strength value until the jumping frequency of the particles in the system coincides with the frequency of the externally applied periodic signal, the SR can be generated.

B. Overview of DSR

DSR is an iterative form of SR, which is more suitable for HSI processing. Its expression is as follows:

$$x(d+1) = x(d) + h[ax(d) - bx^3(d) + f(t) + \xi(t)] \quad (4)$$

where h denotes the step size of the iteration and d is the number of iterations.

The HSI is a three-dimensional tensor that comprises a one-dimensional spectral vector and two-dimensional spatial image information. For a specific HSI with height, width, and number of bands represented as H, W, and N, respectively, the spectral dimension vector at the (i, j) spatial position can be expressed as $A_{i,j} = \{A_{i,j,1}, A_{i,j,2}, A_{i,j,3}, \dots, A_{i,j,N}\}$, where (i=1,2,3,..., H; j=1,2,3, ..., W). The spatial information of the n-th band can be described as $B_n^{H \times W} = \{B_1^{H \times W}, B_2^{H \times W}, B_3^{H \times W}, \dots, B_n^{H \times W}, \dots, B_N^{H \times W}\}$. By substituting these expressions into equation (4), one can obtain the spectral enhancement result at (i, j) and the spatial enhancement result of the n-th band after d iterations:

$$x_{spe}(d+1) = x_{spe}(d) + h[ax_{spe}(d) - bx_{spe}^3(d) + A_{i,j}] \quad (5)$$

$$x_{spa}(d+1) = x_{spa}(d) + h[ax_{spa}(d) - bx_{spa}^3(d) + B_n^{H \times W}] \quad (6)$$

C. Overview of 3D-CNN

The CNN is widely recognized as one of the most effective methods for image classification [23]. The three-dimensional feature of 3D-CNN is particularly advantageous for extracting and classifying spectral-space features in HSIs represented as a three-dimensional tensor. A typical 3D-CNN network structure consists of an Input Layer, Convolutional Layer, Pooling Layer, Fully-Connected Layer, and Output Layer, as illustrated in Figure 2.

In the 3D-CNN architecture, Layer 1 functions as the input layer that takes in a 3D tensor.

The core of 3D-CNN architecture is the convolutional layer, responsible for feature extraction. Compared to 2D-CNN, the 3D-CNN's multi-layer convolutional operation is capable of extracting more complex features. In particular, the input data is feature mapped using 3D convolutional kernels. The resulting value at pixel location (x, y, z) on the n-th feature map in the k-th layer can be calculated using equation (7) [12]:

$$\theta_{kn}^{xyz} = f\left(\sum_m \sum_{\alpha=0}^{\alpha-1} \sum_{\beta=0}^{\beta-1} \sum_{\gamma=0}^{\gamma-1} w_{knm}^{\alpha\beta\gamma} \theta_{(k-1)n}^{(x+\alpha)(y+\beta)(z+\gamma)} + r_{kn}\right) \quad (7)$$

where θ_{kn}^{xyz} represents the output at the position (x, y, z) in the n-th feature map of the layer k (k denotes the current layer), f is the activation function, m is the set of features connected to the current feature map on the (k-1)-th layer, and α , β , and γ are the height, width, and depth of the kernel, respectively. The weight value $w_{knm}^{\alpha\beta\gamma}$ at the position (α, β, γ) is connected to the n-th feature map, and r represents the offset.

To mitigate the vanishing or exploding gradient issues, this paper adopts rectified linear units (ReLUs) as the activation function [24].

The pooling layer subsamples the feature maps, reducing the size of data units and network parameters. In this work, max-pooling [25] is used to retain more texture information in HSIs.

The fully-connected layer is responsible for connecting all features and transforming them into a one-dimensional vector, which is then sent to the classifier for classification. In this study, softmax regression is employed as the classifier, which enables the visualization of the probability distribution of the labels.

III. PROPOSED IMPROVEMENT

A. Principle of the improved algorithm D-DSR

Each pixel in an HSI, being a three-dimensional tensor, exhibits a certain degree of correlation with its neighboring pixels in the spatial dimension. However, traditional DSR algorithms sample the image from only one direction, leading to an incomplete utilization of this correlation. To address this issue, this paper proposes a D-DSR algorithm based on the bistatic system, which employs two consecutive DSRs to sample the image along two different row and column directions. This allows for the retention of more image information and leads to better enhancement results. In contrast to general two-dimensional grayscale images, where grayscale values range from 0 to 255, the adiabatic approximation theory [26] and linear response theory [27] require small parameters to be substituted - that is, the signal's amplitude, frequency, and noise intensity should be much less than 1. Therefore, prior to performing SR, the HSI grayscale values must be linearly normalized to the range of [0,1]. Finally, the D-DSR algorithm's effectiveness in enhancing the shadow region is evaluated by measuring the HSI classification accuracy. The experimental steps of the D-DSR algorithm for enhancing the shaded part of HSI are presented below, with the corresponding flow chart shown in Figure 3.

Step1: The original dataset is pre-processed by removing bands and linearly normalizing the grayscale values of HSI pixels to the range of [0,1]. A mask is used to extract only the shadowed regions, which are enhanced without affecting the non-shadowed areas.

Step2: The HSI is continuously sampled in line scan mode in the spatial dimension and expanded into a 1D-signal. This signal is then sequentially processed through a bistable nonlinear system to obtain a set of SR sequences.

Step3: The sequence output from the system is reconstructed into a square array by line scan. However, the pixel histogram of the grayscale image transformed by the square matrix is concentrated in a narrow range, which increases image brightness but decreases contrast, resulting in a lack of precise details. To balance the overall distribution of pixel grayscale values in the image, the square matrix is normalized to a grayscale range of [0,1].

Step4: Using the mask, the DSR-enhanced image is obtained by fusing the shaded part with the non-shaded part of the original data.

Step5: The shadow region of each HSI obtained from Step 4 is extracted using the shadow mask, expanded into a 1D-sequence by column scanning, and input into the bistable nonlinear system for the 2nd DSR to obtain a set of sequences.

Step6: The second sequence is reconstructed into a square array in column scan mode, fused with the original HSI's non-shadowed region, and then normalized to the range of [0,1] to obtain a D-DSR enhanced image with an improved shadow region.

Step7: The mean value and standard deviation of the original HSI and the shadow part of the image enhanced by DSR and D-DSR algorithms are compared after applying the mask and setting the non-shaded regions to 0.

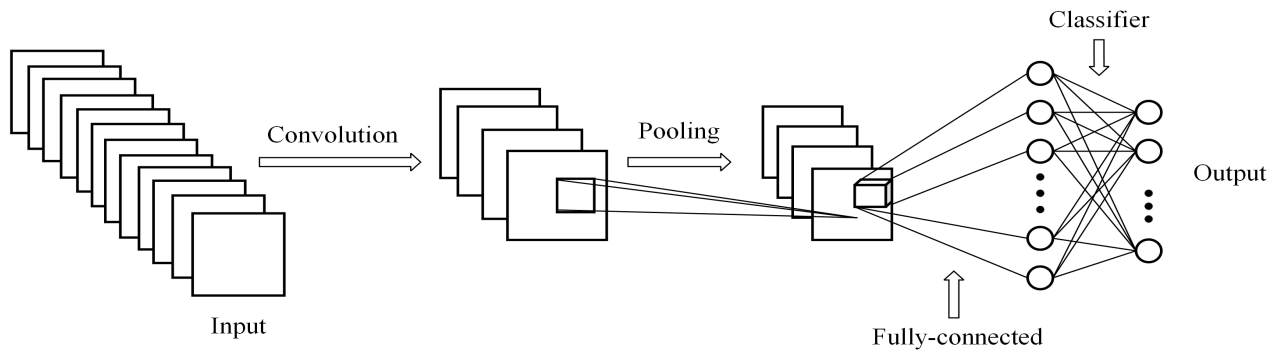


Fig. 2. The main framework of 3D-CNN.

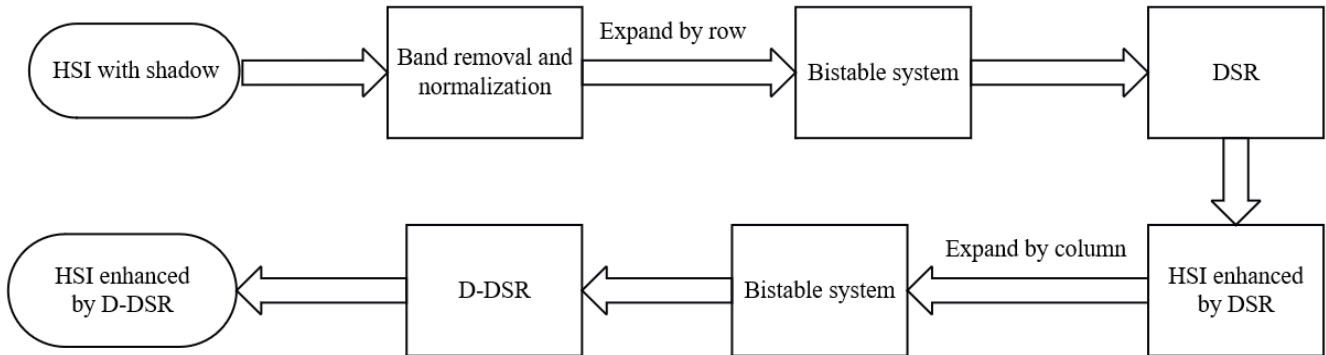


Fig. 3. Main steps of D-DSR for HSI enhancement.

Step8: To assess the effectiveness of D-DSR image enhancement, we optimize the parameters of the 3D-CNN model based on the overall accuracy (OA) of the D-DSR enhanced dataset. We also compare D-DSR with DSR and three commonly used HSI denoising algorithms, namely discrete cosine transform (DCT) [28], weighted nuclear norm minimization (WNNM) [29], and k-means singular value decomposition (K-SVD) [30]. The HSI images processed by these algorithms are then classified using eight methods, including 2D-CNN [31], 3D-CNN, HybridSN [32], 3D-ResNet [23], VGGNet, AlexNet, SVM, and Spectral Angle Mapper (SAM). The classification accuracy is evaluated using two metrics: OA, average accuracy (AA) and Kappa.

B. Parameters optimization of the 3D-CNN classification model

The impact of parameter settings on classification results can be significant. Therefore, in Step8, the parameters of the 3D-CNN classification model are optimized to enhance the performance of the network for HSI after D-DSR enhancement.

Initially, the HSI is fed into the classification model, and parameters are set to default or empirical values [33]. Then, the epoch, batch size, learning rate (LR), optimizer, and loss function are adjusted separately based on the univariate principle [34], while other parameters are held constant when one is modified. Finally, the optimal parameters are selected based on the OA of the 3D-CNN classification results.

To attain the optimal fitting state and improve training accuracy, the epoch is set between 10 and 130, and the most suitable epoch value is chosen based on the OA of the 3D-CNN classification. The batch size refers to the number of samples in the batch data, which is used to train

the model and update the weights in each training process. Increasing the batch size value enhances parallelization efficiency, improves descent direction accuracy, reduces training oscillation, and leads to convergence at an optimal time within a certain range. The learning rate controls the impact of the output error on the network parameters. A smaller learning rate results in slower loss gradient reduction and longer convergence times, but it also reduces the effect of output error on parameters. This paper adopts an exponential decay mechanism for learning rate, and the magnitude of the learning rate corresponding to the relative maximum of OA is selected as the optimal parameter. Adam, an adaptive optimizer with faster and more stable convergence, and Binary Cross-Entropy Loss function, which is more suitable for HYDICE data after D-DSR enhancement, are chosen after comparison experiments of several commonly used optimizers and loss functions.

IV. EXPERIMENTS AND RESULTS

A. Experimental data

We conducted experiments to assess the denoising ability of the D-DSR method in the shadow region of the HSI. This dataset was obtained in August 1995 as part of the Hyperspectral Digital Image Collection Experiment (HYDICE) and contains 148 bands with dimensions of 316 rows and 216 columns, represented by $R^{316 \times 216 \times 148}$. The dataset has a spatial resolution of 0.75m and a spectral resolution of 10nm, with seven land cover categories including field, tree, road, shadow (which includes a section of road), and three different targets. To evaluate the classification performance, we divided the shadow region into two categories: shadow and road under the shadow. Eight types of features were

classified and distinguished by eight different colors, as summarized in Table I.

TABLE I
SAMPLE CATEGORIES AND NUMBERS OF HYDICE.

NO.	Color	Classes	Number of pixels
1		Field	41480
2		Tree	13562
3		Road	4220
4		Road under shadow	2180
5		Target1	671
6		Target2	404
7		Target3	642
8		Shadow	5169
All classes			68256

B. HSI pre-processing

In the HYDICE dataset, certain bands contain less information than others due to various factors such as atmospheric noise and water absorption. To improve the efficiency of image processing, it is necessary to remove these bands [35]. To evaluate the magnitude of energy in each band of the hyperspectral image, we use the Frobenius norm (F-norm), which is defined as the square root of the sum of the squares of all matrix elements. Equation (8) shows how the F-norm for each band of the spectral dimension can be calculated:

$$\|I(:, :, I_3)\|_F = \left(\sum_{i_1=1}^{I_1} \sum_{i_2=1}^{I_2} |I(i_1, i_2, I_3)|^2 \right)^{\frac{1}{2}} \quad (8)$$

where i_1 , i_2 and I_3 denote the number of rows, columns and spectral bands of the HSI.

In Figure 4, the F-norm values of all 148 bands of HYDICE are displayed, indicating that each band contains a significant amount of information, with F-norm values exceeding 9.31. Therefore, there is no need to remove any bands from the dataset. Following this, linear normalization is applied to the HSI.

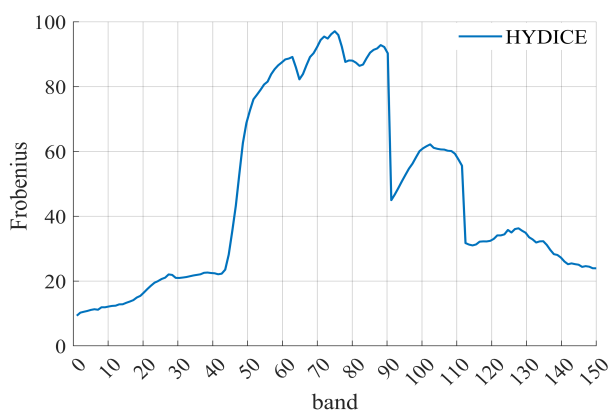


Fig. 4. F-norm for each band of HYDICE.

To evaluate the impact of D-DSR on the enhancement of HSI, a scene with a shadow region was selected from the HYDICE dataset for experimentation, as depicted in Figure 5(a). The shadow mask is shown in Figure 5(b). The scene features were categorized into eight groups, namely field, tree, road, shadow, three different targets, and road under shadow. The ground truth is illustrated in Figure 5(c).

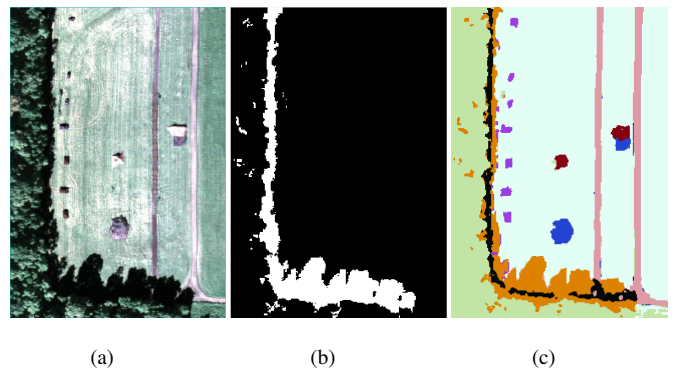


Fig. 5. (a) A scene of HYDICE. (b) Shadow mask. (c) Ground truth.

C. Evaluation index

In this study, we assess the denoising effect of shadow regions in images through both qualitative and quantitative analyses.

The qualitative analysis employs the comparative evaluation method in subjective evaluation: human viewing, which relies on the human eyes to capture image information, analyze and integrate it in the brain. Image quality judgment is influenced by various factors, which can be separately extracted and then synthesized for image quality evaluation. We observe the D-DSR and DSR processed images according to the subjective visual perception of the human eyes, and then compare the image quality.

However, since the human visual system perceives the image non-uniformly and non-linearly, it cannot detect all changes in the picture. Hence, quantitative analysis of image variation is also required. In this study, we use mean value and standard deviation as indicators for quantitative image quality analysis. The mean value is the average value of image pixels, denoted by μ , which reflects the average brightness of the image. The greater the brightness, the better the image quality. The standard deviation is the degree of dispersion of the grayscale of image pixels relative to the mean value and is denoted by STD. If the standard deviation is higher, the gray levels in the image are more dispersed, and the image quality is better. We calculate the mean value and standard deviation using equations (9) and (10), respectively:

$$\mu = \frac{1}{MN} \sum_{i=1}^M \sum_{j=1}^N F(i, j) \quad (9)$$

$$\text{STD} = \sqrt{\frac{1}{MN} \sum_{i=1}^M \sum_{j=1}^N [F(i, j) - \mu]^2} \quad (10)$$

where F is the image with the size of $M \times N$, (i, j) is the pixel's position in the image.

The discrete entropy indicates the amount of information content in the image, which is denoted by E as:

$$E = - \sum_g^{G-1} p(f) \log_2 p(f) \quad (11)$$

where G indicates the maximum value of the gray level, $p(f)$ denotes the probability that the pixel value f appears in the 3D image.

In the context of HSI denoising, the primary objective is to enhance target detection and image classification accuracy.

This paper uses two metrics, OA and Kappa, to measure classification accuracy. OA is defined as the ratio of the number of correctly classified pixels to the total number of pixels across all categories. The meaning of AA is the mean value of the percentage of samples correctly classified. Kappa, on the other hand, is used to represent the proportion of error reduction generated by the classification compared to a completely random sort. OA and Kappa are calculated according to the following equations:

$$OA = \frac{1}{N} \sum_{i=1}^C x_{ii} \times 100\% \quad (12)$$

$$AA = \frac{1}{C} \sum_c \frac{x_{ii}}{\sum_j x_{ij}} \times 100\% \quad (13)$$

$$Kappa = \frac{N \sum_{i=1}^C x_{ii} - \sum_{i=1}^C (x_{i+} \cdot x_{+i})}{N^2 - \sum_{i=1}^C (x_{i+} \cdot x_{+i})} \times 100\% \quad (14)$$

where N and C are the total numbers of samples and categories in the HSI, x_{ii} is the number of correctly classified test samples, x_{ij} denotes the number of misclassified samples. x_{i+} is the number of actual samples per category, and x_{+i} is the number of predicted samples per category.

D. D-DSR algorithm to enhance HSI

The bistable nonlinear system's parameters are set to optimal values of $a=0.01$ and $b=0.01$ [36]. The sampling frequency f_s is set to 1000, and the step size is $h = \frac{1}{f_s} = 0.001$. The first band of the original HSI as illustrated in Figure 6(a). Then it is enhanced using the DSR and D-DSR methods in the spatial dimension, respectively. The results of band one are displayed in Figure 6(b) and Figure 6(c). A shadow extraction mask is fused with the original HSI and the enhanced HSI, and the mean value and standard deviation of the resulting images are calculated separately. Visual examination of Figure 6 and Figure 7 indicate that the D-DSR-enhanced images with clearer and richer details in the shadow region than the DSR-enhanced image, with increased brightness.

To evaluate the impact of different sampling methods on DSR and D-DSR, column and row scans are replaced row and column scans at Steps 2, 3, 5, and 6. Comparisons are made of the mean value, standard deviation and discrete entropy of images in band 1 before and after the replacement, as well as the classification accuracy OA and Kappa (3D-CNN classification with 20% of the total training samples), as shown in Table II. The experimental data demonstrate that the effects of row-scan and column-scan methods on DSR and D-DSR are not significantly different. From the table, it can be also seen that the evaluation indexes of the image enhanced by D-DSR are better than those of DSR and the original image, indicating that the D-DSR method helps to improve the quality of HSI.

Figures 8 and 9 provide a comparison of the spectral information of the original HSI, DSR, and the D-DSR enhanced dataset. The mean value of the spectra of the pixel points in the corresponding area is taken separately for each

spectrum segment. It is evident that the spectral information features of the shaded areas and the shady roads are more visible after D-DSR processing, with more remarkable spectral reflections compare to before the processing and after DSR enhancement.

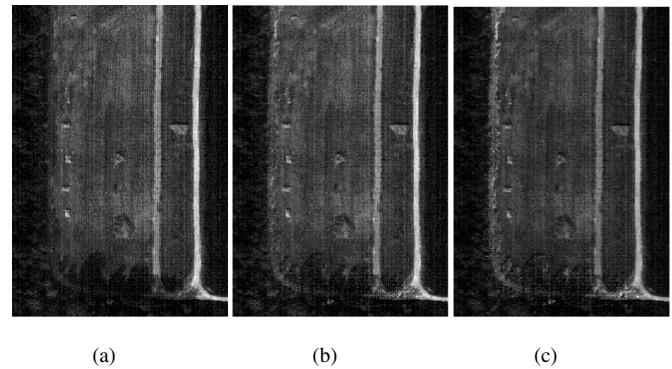


Fig. 6. The 1st band of images in the spatial dimension. (a) Original HSI. (b) HSI after DSR enhancement. (c) HSI after D-DSR enhancement.

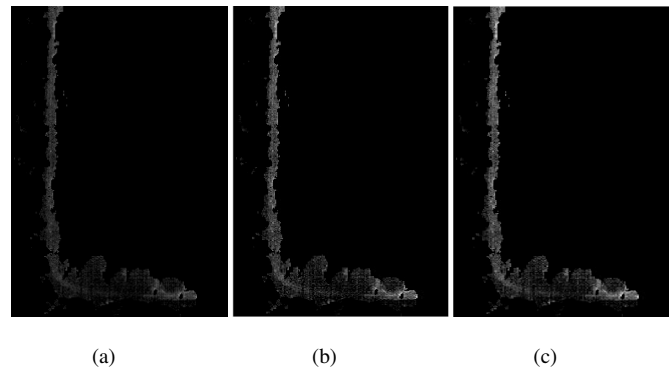


Fig. 7. The 1st band of shadow area in the spatial dimension. (a) Original HSI. (b) HSI after DSR enhancement. (c) HSI after D-DSR enhancement.

TABLE II
MEAN VALUES AND STANDARD DEVIATIONS OF THE ORIGINAL HSI AND THE HSI AFTER DSR AND D-DSR ENHANCEMENT WITH DIFFERENT SAMPLING METHODS IN THE 1ST BAND.

	Original data	DSR(row scan)	D-DSR(column scan)	DSR(column scan)	D-DSR(row scan)
μ	839.1554	1288.7000	1448.8000	1288.7000	1444.4000
Std	2978.0000	4632.1000	5219.4000	4632.1000	5229.0000
E	6.5367	6.7884	6.8942	6.7271	6.8735
OA	96.5433	97.0300	97.2411	97.0274	97.2454
Kappa	94.0223	94.8845	95.2496	94.8369	95.2408

E. HSI classification

In this study, four HSI denoising algorithms, namely K-SVD, DCT, WNNM, and DSR, are utilized in the spatial dimension for comparison experiments. The resulting enhanced images are then classified using various methods, including 2D-CNN, 3D-CNN, HybridSN, 3D-ResNet, VGGNet, and AlexNet, all of which are based on CNN models [12, 37].

The 2D-CNN algorithm extracts only the 2D spatial features of the image and requires dimensionality reduction when processing HSI. On the other hand, 3D-CNN can extract both spectral and spatial features of HSI. HybridSN

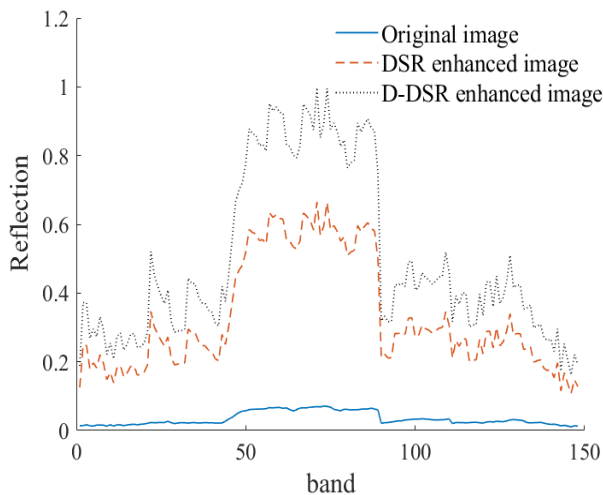


Fig. 8. The spectral information of shadow area before and after enhancement.

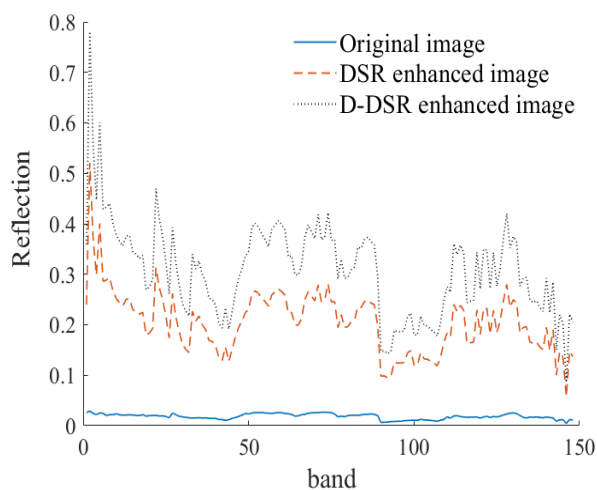


Fig. 9. The spectral information of the road under shadow before and after enhancement.

is a hybrid spectral CNN that incorporates spatial-spectral features, addressing the drawback of 2D-CNN not being able to extract good recognition feature mapping from the spectral dimension, and has lower model complexity than 3D-CNN but cannot fully utilize the spectral information of the joint space. By fusing ResNet and 3D-CNN and using the residual structure to connect 3D-CNN modules, 3D-ResNet solves the problems of vanishing gradient and exploding gradient of deep networks, allowing the network layers to become deeper. VGGNet has a simple structure but a large number of parameters, while AlexNet is a single-branch network structure that makes extensive use of data expansion techniques and uses the ReLU activation function for the first time, with better gradient characteristics and faster training.

In addition to CNN-based methods, two non-CNN classification methods, namely SAM and SVM, are also employed according to the univariate principle. SVM is suitable for small and medium-sized samples, nonlinear, and high-dimensional classification problems, while SAM determines the class of the test sample by calculating the spectral angle similarity between the test sample and the training sample.

1) *Experiments for parameter optimization of 3D-CNN classification:* The parameters of 3D-CNN are optimized based on the steps outlined in Section 3.2, and the same approach is employed for the optimization of the other three comparative classification models used in this study. The results of these experiments are presented in Figure 10, Figure 11, Figure 12, Table III, and Table IV. As a control, the same procedure is used to optimize the parameters of the unenhanced original HYDICE data, and the results are shown in Figure 13, Figure 14, Figure 15, Table V, and Table VI. In the case of D-DSR enhanced HYDICE, the classification ability of 3D-CNN is verified by using the same parameter values for all CNN classification methods employed in this study, as detailed in Table VII.

2) *Classification results:* The classification results of different percentages of training data in the sample are presented in Table VIII to Table XV, showing the OA and Kappa values averaged over ten results after removing the singular values. Figure 16 compares the AA values after the classification of the images by all considered algorithms. As an example, Figure 17 to Figure 24 display the classification results for the training set comprising 20% of the samples. To evaluate the classification performance of the proposed algorithm, the original images and the images enhanced by the five enhancement methods are classified, and the accuracy of each category is calculated. The results are tabulated in Table XVI to Table XXIII.

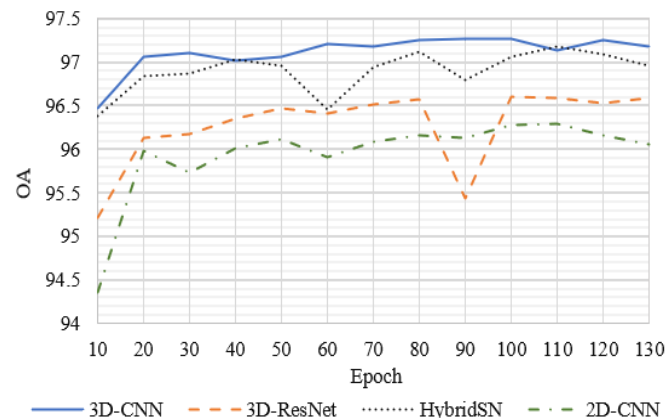


Fig. 10. OA with different epochs in all classification methods (HYDICE data after D-DSR enhancement).

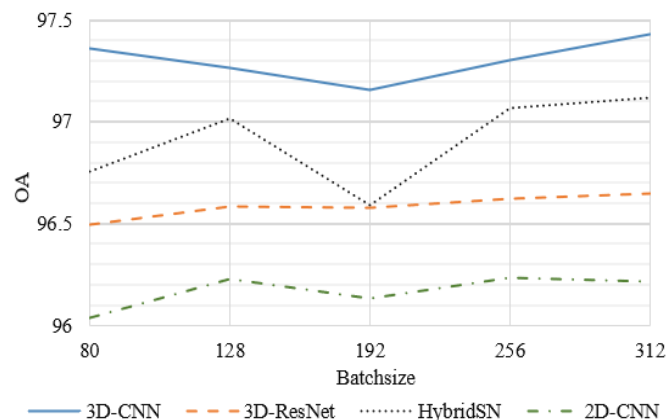


Fig. 11. OA with different batchsizes in all classification methods (HYDICE data after D-DSR enhancement).

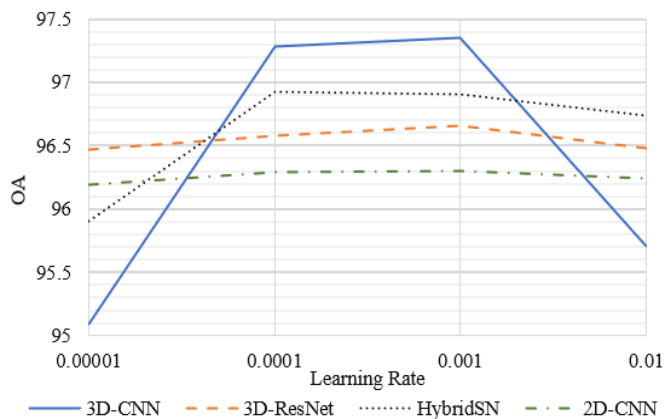


Fig. 12. OA with different learning rates in all classification methods (HYDICE data after D-DSR enhancement).

TABLE III

OA WITH DIFFERENT OPTIMIZERS IN ALL CLASSIFICATION METHODS (HYDICE DATA AFTER D-DSR ENHANCEMENT).

optimizer	3D-CNN	3D-ResNet	HybridSN	2D-CNN
Adam	97.3042	96.6017	97.1229	96.1322
RMSProp	96.7145	96.4179	97.1009	95.9747
SGD	96.6999	96.1212	96.8281	95.4564
AdaGrad	95.0883	94.8704	95.3813	92.4366
AdaDelta	87.0323	78.3737	60.7709	83.7963

TABLE IV

OA WITH DIFFERENT LOSSES IN ALL CLASSIFICATION METHODS (HYDICE DATA AFTER D-DSR ENHANCEMENT).

Loss	3D-CNN	3D-ResNet	HybridSN	2D-CNN
Categorical Cross Entropy	97.3464	96.5241	97.1010	96.2860
Hinge	93.2002	60.7709	60.7709	92.1545
Binary Cross-Entropy	97.3665	96.7054	97.1705	96.3666
KL-divergence	97.1486	95.9417	96.9233	96.2878

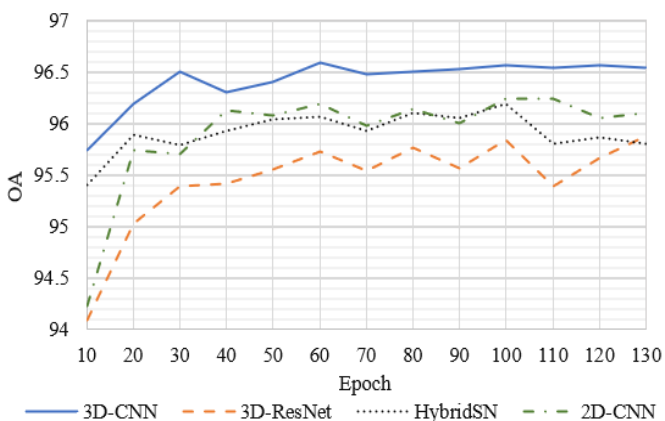


Fig. 13. OA with different epochs in all classification methods (original HYDICE data).

TABLE V

OA WITH DIFFERENT OPTIMIZERS IN ALL CLASSIFICATION METHODS (ORIGINAL HYDICE DATA).

optimizer	3D-CNN	3D-ResNet	HybridSN	2D-CNN
Adam	96.7402	96.0498	95.7183	96.1944
RMSProp	96.3483	95.5315	95.7879	95.7989
SGD	95.9033	95.1872	96.1065	94.3356
AdaGrad	93.8558	93.7514	94.0609	92.1142
AdaDelta	80.8881	76.3373	60.7709	83.9263

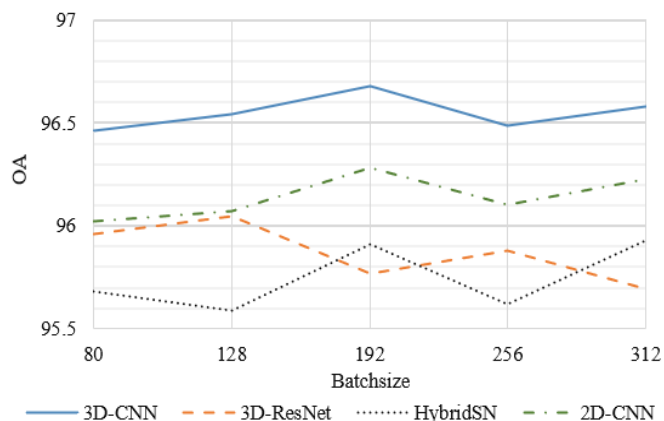


Fig. 14. OA with different batchsizes in all classification methods (original HYDICE data).

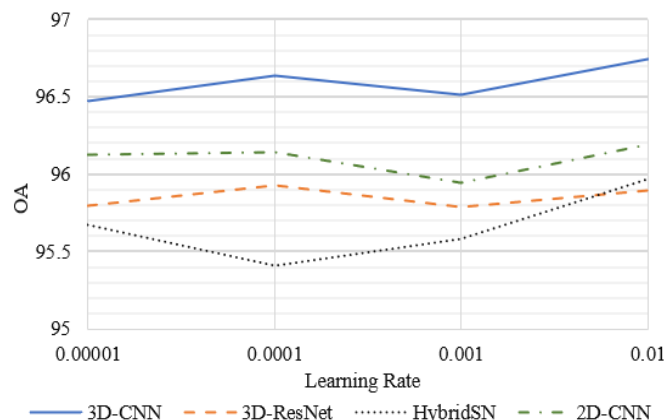


Fig. 15. OA with different learning rates in all classification methods (original HYDICE data).

TABLE VI

OA WITH DIFFERENT LOSSES IN ALL CLASSIFICATION METHODS (ORIGINAL HYDICE DATA).

Loss	3D-CNN	3D-ResNet	HybridSN	2D-CNN
Categorical Cross Entropy	96.7402	96.0498	96.2952	96.1944
Hinge	86.4481	60.7709	60.7709	90.8891
Binary Cross-Entropy	96.6303	95.9637	88.2904	96.1267
KL-divergence	96.6010	95.9912	96.0840	96.2036

TABLE VII

PARAMETERS OF THE CLASSIFICATION METHODS USED IN THIS PAPER.

Method	Epoch	Batch Size	Learning Rate	Loss	Optimizer
AlexNet	100	312	0.001	Binary Cross-Entropy	Adam
VGGNet	100	312	0.001	Binary Cross-Entropy	Adam
2D-CNN	100	312	0.001	Binary Cross-Entropy	Adam
3D-ResNet	100	312	0.001	Binary Cross-Entropy	Adam
HybridSN	100	312	0.001	Binary Cross-Entropy	Adam
3D-CNN	100	312	0.001	Binary Cross-Entropy	Adam

TABLE VIII
OA AND KAPPA OF SVM CLASSIFICATION METHODS FOR ALL DATA.

Training Data Percentage	Original Data		DCT		WNNM		K-SVD		DSR on Spatial Dimension		D-DSR on Spatial Dimension		DSR on Spectral Dimension	
	OA	Kappa	OA	Kappa	OA	Kappa	OA	Kappa	OA	Kappa	OA	Kappa	OA	Kappa
	15%	95.1120	91.5348	95.1059	91.5136	95.1454	91.5989	95.1409	91.5803	95.1551	91.6025	95.1791	91.6567	95.1868
20%	95.6434	92.4811	95.6430	92.4807	95.6875	92.5630	95.6871	92.5624	95.6903	92.5882	95.6982	92.6063	95.7045	92.6106
25%	95.9337	92.9672	95.9329	92.9667	95.9508	93.0068	95.9501	93.0053	95.9661	93.0266	95.9687	93.0304	95.9819	93.0678

TABLE IX
OA AND KAPPA OF SAM CLASSIFICATION METHODS FOR ALL DATA.

Training Data Percentage	Original Data		DCT		WNNM		K-SVD		DSR on Spatial Dimension		D-DSR on Spatial Dimension		DSR on Spectral Dimension	
	OA	Kappa	OA	Kappa	OA	Kappa	OA	Kappa	OA	Kappa	OA	Kappa	OA	Kappa
	15%	95.2744	91.8261	95.3018	91.8872	95.2662	91.8033	95.8630	92.8936	95.8579	92.8725	95.9621	93.1201	95.9451
20%	95.6281	92.4463	95.6904	92.5662	95.6357	92.4689	96.0550	93.1879	96.0485	93.1665	96.1821	93.4189	95.0644	93.1254
25%	95.8776	92.8880	95.9103	92.9623	95.8957	92.9201	96.2565	93.5647	96.2484	93.5240	96.4770	93.9529	96.3005	93.6462

TABLE X
OA AND KAPPA OF ALEXNET CLASSIFICATION METHODS FOR ALL DATA.

Training Data Percentage	Original Data		DCT		WNNM		K-SVD		DSR on Spatial Dimension		D-DSR on Spatial Dimension		DSR on Spectral Dimension	
	OA	Kappa	OA	Kappa	OA	Kappa	OA	Kappa	OA	Kappa	OA	Kappa	OA	Kappa
	15%	95.3737	92.0030	95.6340	92.4587	95.4044	92.0544	95.9710	93.0335	95.9499	92.9720	96.0842	93.2346	95.9800
20%	95.7437	92.6872	96.1077	93.2781	95.8832	92.8906	96.2081	93.4522	96.1972	93.4301	96.2518	93.5389	96.2362	93.4980
25%	96.1079	93.2785	96.3716	93.7434	96.3462	93.6881	96.4590	93.8749	96.4457	93.8610	96.5234	93.9929	96.4892	93.9462

TABLE XI
OA AND KAPPA OF 2D-CNN CLASSIFICATION METHODS FOR ALL DATA.

Training Data Percentage	Original Data		DCT		WNNM		K-SVD		DSR on Spatial Dimension		D-DSR on Spatial Dimension		DSR on Spectral Dimension	
	OA	Kappa	OA	Kappa	OA	Kappa	OA	Kappa	OA	Kappa	OA	Kappa	OA	Kappa
	15%	95.6783	92.5441	95.6599	92.5224	95.7082	92.6143	95.7003	92.5921	95.6979	92.5913	95.7064	92.6035	95.8958
20%	96.1734	93.4308	96.1945	93.3777	96.2375	93.5182	96.1801	93.4169	96.2116	93.4725	96.2662	93.5584	96.3184	93.6511
25%	96.4374	93.8635	96.5557	94.0668	96.5779	94.1125	96.5100	93.9884	96.5146	94.0065	96.6028	94.1465	96.5410	94.0339

TABLE XII
OA AND KAPPA OF VGGNET CLASSIFICATION METHODS FOR ALL DATA.

Training Data Percentage	Original Data		DCT		WNNM		K-SVD		DSR on Spatial Dimension		D-DSR on Spatial Dimension		DSR on Spectral Dimension	
	OA	Kappa	OA	Kappa	OA	Kappa	OA	Kappa	OA	Kappa	OA	Kappa	OA	Kappa
	15%	95.5835	92.3573	95.6674	92.5126	95.2973	91.8562	95.8260	92.7874	95.8125	92.7632	95.9712	93.0439	95.9037
20%	95.9434	92.9603	96.0162	93.1205	95.7082	92.6073	96.2307	93.5046	96.2216	93.4829	96.3728	93.7464	96.3196	93.6536
25%	96.2489	93.5266	96.3201	93.6584	96.0027	93.1043	96.5273	94.0027	96.5182	93.9873	96.6528	94.2578	96.5853	94.1159

TABLE XIII
OA AND KAPPA OF 3D-RESNET CLASSIFICATION METHODS FOR ALL DATA.

Training Data Percentage	Original Data		DCT		WNNM		K-SVD		DSR on Spatial Dimension		D-DSR on Spatial Dimension		DSR on Spectral Dimension	
	OA	Kappa	OA	Kappa	OA	Kappa	OA	Kappa	OA	Kappa	OA	Kappa	OA	Kappa
	15%	95.4310	92.1106	95.6637	92.5002	95.3508	91.9733	95.9760	93.0437	95.9064	92.9425	96.1595	93.3696	96.0871
20%	95.8352	92.8174	96.2068	93.4488	95.8489	92.8297	96.4779	93.9203	96.3384	93.6785	96.6017	94.1382	96.3669	93.7355
25%	96.0320	93.1635	96.5062	93.9752	96.2683	93.5689	96.6237	94.1909	96.5319	94.0170	96.9831	94.8014	96.8193	94.5188

TABLE XIV
OA AND KAPPA OF HYBRIDSN CLASSIFICATION METHODS FOR ALL DATA.

Training Data Percentage	Original Data		DCT		WNNM		K-SVD		DSR on Spatial Dimension		D-DSR on Spatial Dimension		DSR on Spectral Dimension	
	OA	Kappa	OA	Kappa	OA	Kappa	OA	Kappa	OA	Kappa	OA	Kappa	OA	Kappa
	15%	95.5593	92.3278	96.1541	93.3555	95.6360	92.4627	96.6040	94.1482	96.6813	94.2786	96.8056	94.4874	96.4740
20%	96.1056	93.2747	96.4014	93.7844	96.0739	93.2190	96.9406	94.7288	96.9465	94.7377	97.0654	94.9361	96.7739	94.4320
25%	96.2604	93.5474	96.7681	94.4270	96.3574	93.7087	97.2180	95.2091	97.1157	95.0216	97.2750	95.2989	97.1346	95.0548

TABLE XV
OA AND KAPPA OF 3D-CNN CLASSIFICATION METHODS FOR ALL DATA.

Training Data Percentage	Original Data		DCT		WNNM		K-SVD		DSR on Spatial Dimension		D-DSR on Spatial Dimension		DSR on Spectral Dimension	
	OA	Kappa	OA	Kappa	OA	Kappa	OA	Kappa	OA	Kappa	OA	Kappa	OA	Kappa
	15%	96.2853	93.6006	96.3644	93.7359	95.4905	92.2274	97.0672	94.9462	96.7481	94.3934	97.2008	95.1792	96.7445
20%	96.5433	94.0223	96.5565	94.0665	95.7537	92.6696	97.1589	95.1070	97.0300	94.8845	97.3664	95.4496	96.9746	94.7752
25%	96.7052	94.3233	96.8000	94.4874	96.2829	93.5890	97.4588	95.6144	97.2027	95.1785	97.6148	95.8945	97.3765	95.4757

TABLE XVI
ACCURACY OF EACH CATEGORY AFTER SVM CLASSIFICATION.

Method	Original Data	DCT	WNNM	K-SVD	DSR	D-DSR
Field	0.9750	0.9755	0.9750	0.9750	0.9750	0.9750
Tree	0.9340	0.9360	0.9350	0.9390	0.9375	0.9375
Road	0.9410	0.9425	0.9480	0.9460	0.9475	0.9470
Road under shadow	0.7070	0.6825	0.6940	0.7360	0.7400	0.7655
Shadow	0.8000	0.7740	0.7780	0.8520	0.8480	0.8565
Target 1	0.8035	0.8270	0.8030	0.8440	0.8440	0.8435
Target 2	0.7050	0.7080	0.7190	0.7430	0.7455	0.7435
Target 3	0.8210	0.8110	0.8255	0.8465	0.8455	0.8450

TABLE XIX
ACCURACY OF EACH CATEGORY AFTER 2D-CNN CLASSIFICATION.

Method	Original Data	DCT	WNNM	K-SVD	DSR	D-DSR
Field	0.9900	0.9900	0.9900	0.9900	0.9900	0.9900
Tree	0.9560	0.9600	0.9680	0.9640	0.9655	0.9670
Road	0.9610	0.9625	0.9700	0.9670	0.9685	0.9670
Road under shadow	0.7890	0.7985	0.7980	0.8020	0.8060	0.8095
Shadow	0.9200	0.8755	0.8615	0.9300	0.9350	0.9450
Target 1	0.8435	0.8620	0.8340	0.9240	0.9000	0.9015
Target 2	0.7620	0.7580	0.7830	0.8520	0.8090	0.8135
Target 3	0.8710	0.8680	0.8695	0.8545	0.8695	0.8480

TABLE XVII
ACCURACY OF EACH CATEGORY AFTER SAM CLASSIFICATION.

Method	Original Data	DCT	WNNM	K-SVD	DSR	D-DSR
Field	0.9760	0.9760	0.9750	0.9760	0.9760	0.9760
Tree	0.9450	0.9460	0.9355	0.9480	0.9475	0.9475
Road	0.9470	0.9475	0.9480	0.9470	0.9475	0.9470
Road under shadow	0.7370	0.7235	0.7180	0.7400	0.7500	0.7655
Shadow	0.8400	0.8240	0.8340	0.8540	0.8550	0.8755
Target 1	0.8230	0.8300	0.8200	0.8470	0.8460	0.8455
Target 2	0.7250	0.6980	0.8000	0.7450	0.7465	0.7445
Target 3	0.8320	0.8460	0.8250	0.8465	0.8455	0.8455

TABLE XX
ACCURACY OF EACH CATEGORY AFTER VGGNET CLASSIFICATION.

Method	Original Data	DCT	WNNM	K-SVD	DSR	D-DSR
Field	0.9900	0.9900	0.9900	0.9900	0.9900	0.9900
Tree	0.9565	0.9620	0.9640	0.9655	0.9650	0.9665
Road	0.9620	0.9640	0.9680	0.9690	0.9685	0.9680
Road under shadow	0.7905	0.8005	0.7785	0.8320	0.8370	0.8425
Shadow	0.9110	0.9255	0.8215	0.9300	0.9380	0.9470
Target 1	0.8455	0.8645	0.8345	0.9210	0.9000	0.9015
Target 2	0.7630	0.7780	0.7830	0.8020	0.8030	0.8105
Target 3	0.8670	0.8810	0.8015	0.8845	0.8895	0.8880

TABLE XVIII
ACCURACY OF EACH CATEGORY AFTER ALEXNET CLASSIFICATION.

Method	Original Data	DCT	WNNM	K-SVD	DSR	D-DSR
Field	0.9760	0.9760	0.9700	0.9760	0.9860	0.9800
Tree	0.9530	0.9530	0.9450	0.9480	0.9555	0.9560
Road	0.9590	0.9595	0.9620	0.9640	0.9605	0.9600
Road under shadow	0.7880	0.7835	0.7860	0.7960	0.8100	0.8115
Shadow	0.8800	0.8840	0.9750	0.8995	0.9240	0.9300
Target 1	0.8430	0.8800	0.8700	0.8920	0.8860	0.8850
Target 2	0.7440	0.6980	0.7390	0.7650	0.7460	0.7455
Target 3	0.8480	0.8560	0.8430	0.8560	0.8450	0.8430

TABLE XXI
ACCURACY OF EACH CATEGORY AFTER 3D-RESNET CLASSIFICATION.

Method	Original Data	DCT	WNNM	K-SVD	DSR	D-DSR
Field	0.9900	0.9880	0.9900	0.9900	0.9900	0.9900
Tree	0.9545	0.9670	0.9710	0.9785	0.9740	0.9820
Road	0.9600	0.9645	0.9490	0.9670	0.9565	0.9570
Road under shadow	0.7915	0.8020	0.7590	0.8350	0.8390	0.8415
Shadow	0.9200	0.9470	0.9410	0.9485	0.9470	0.9495
Target 1	0.8920	0.8955	0.9000	0.8970	0.8415	0.8810
Target 2	0.7540	0.8780	0.7540	0.7780	0.8050	0.7680
Target 3	0.8650	0.8840	0.8345	0.8655	0.8880	0.8830

TABLE XXII
ACCURACY OF EACH CATEGORY AFTER HYBRIDSN CLASSIFICATION.

Method	Original Data	DCT	WNNM	K-SVD	DSR	D-DSR
Field	0.9800	0.9850	0.9800	0.9900	0.9900	0.9880
Tree	0.9700	0.9840	0.9800	0.9870	0.9870	0.9820
Road	0.9730	0.9555	0.9700	0.9655	0.9665	0.9700
Road under shadow	0.8105	0.8420	0.7285	0.8510	0.8620	0.8580
Shadow	0.9030	0.9170	0.9400	0.8985	0.9390	0.9390
Target 1	0.9315	0.8780	0.9300	0.8950	0.8980	0.9010
Target 2	0.8640	0.9000	0.8850	0.8080	0.8210	0.8190
Target 3	0.8520	0.8810	0.8025	0.8850	0.8880	0.8900

TABLE XXIII
ACCURACY OF EACH CATEGORY AFTER 3D-CNN CLASSIFICATION.

Method	Original Data	DCT	WNNM	K-SVD	DSR	D-DSR
Field	0.9900	0.9900	0.9900	0.9900	0.9900	0.9900
Tree	0.9730	0.9725	0.9700	0.9810	0.9785	0.9890
Road	0.9700	0.9685	0.9700	0.9690	0.9710	0.9730
Road under shadow	0.8060	0.8420	0.7485	0.8450	0.8530	0.8645
Shadow	0.9200	0.8975	0.9125	0.8995	0.9336	0.9435
Target 1	0.9025	0.8990	0.9310	0.8995	0.9180	0.8990
Target 2	0.7480	0.6895	0.8230	0.6880	0.7490	0.7700
Target 3	0.8920	0.9130	0.8120	0.9140	0.9135	0.9095

V. DISCUSSION

Based on the results of the parameter optimization experiments of 3D-CNN, it is evident that the 3D-CNN classification method achieves higher OA than other methods with the same parameter settings when different classification models are applied to the same data. This suggests that 3D-CNN classification has superior classification capabilities and is better suited for HYDICE data after D-DSR enhancement.

As shown in Table VIII-Table XV, the classification accuracy of all HYDICE data increases as the percentage of training samples increases. The classification accuracies of DSR-enhanced spectral-dimensional and spatial-dimensional images are similar in 3D-CNN, HybridSN, and 3D-ResNet classification methods, but both are lower than those of D-DSR-enhanced spatial-dimensional images when the number of training samples is the same. However, for the 2D-CNN

classification method, this conclusion is only consistent when there are a sufficient number of training set samples. As seen from Table XI, the classification accuracy of DSR-enhanced spectral-dimensional images is higher than that of D-DSR-enhanced spatial-dimensional images when the number of training samples is 20% and 15%. It is noteworthy that when the number of training samples is 15%, the OA and Kappa values of the classification accuracy of HSI enhanced by DSR, D-DSR, K-SVD, and DCT algorithms are not satisfactory, with OA values close to 95.7% and Kappa close to 92.6%, making it difficult to achieve a substantial improvement. These findings are attributed to the 2D-CNN’s inability to fully utilize the 3D tensor property of HSI, which disrupts the correlation between adjacent pixels.

The images and tables demonstrate that the D-DSR algorithm effectively improves the classification accuracy of HSIs in the spatial dimension, outperforming other algorithms such as DSR, K-SVD, DCT, and WNNM. In addition, the results highlight the superior performance of deep learning-based methods, specifically 3D-CNN, over 2D-CNN, HybridSN, and 3D-ResNet classification methods, and the accuracy advantage of CNN-based classification methods over general-purpose methods. The D-DSR algorithm proposed in this study shows particular benefits in extracting shadow information and classifying HSIs containing shadow regions with different targets.

However, while D-DSR is effective in spatial data processing, it does not fully utilize spectral information. Therefore, these findings encourage further exploration of enhancement methods that can leverage both spectral and spatial information, thus fully utilizing the three-dimensional features of HSIs.

VI. CONCLUSIONS

In hyperspectral imaging, shadow regions are challenging for pixel classification due to low illumination, low reflectance, and a small number of trainable samples. This paper proposes the D-DSR algorithm to enhance shadow regions in HSIs, improving their classification accuracy and simplifying information processing. The D-DSR algorithm enhances the shadow region in the spatial dimension using two different sampling methods of DSR, making the HSI consistent in the horizontal and vertical directions of texture enhancement, and restoring the original image information. The enhanced image is then fused with the non-shadow area of the original HSI and classified using the optimized 3D-CNN classification method. Experimental results show that D-DSR outperforms DSR and other denoising methods in improving shadow regions of HSIs, and its classification accuracy is higher when the same method is used. Parameter optimization of the 3D-CNN model achieves higher OA and Kappa in classifying HSI after D-DSR enhancement. Thus, the proposed method has significant potential for application in shadow information extraction and classification of HSIs.

REFERENCES

[1] H. X. Dou, X. M. Pan and C. Wang, “Spatial and Spectral-Channel Attention Network for Denoising on Hyperspectral Remote Sensing Image,” *Remote Sensing*, vol. 14, no. 14, pp. 3338, 2022.
 [2] D. Landgrebe, “Hyperspectral Image Data Analysis,” *IEEE Signal Processing Magazine*, vol. 19, no. 1, pp. 17–28, 2022.

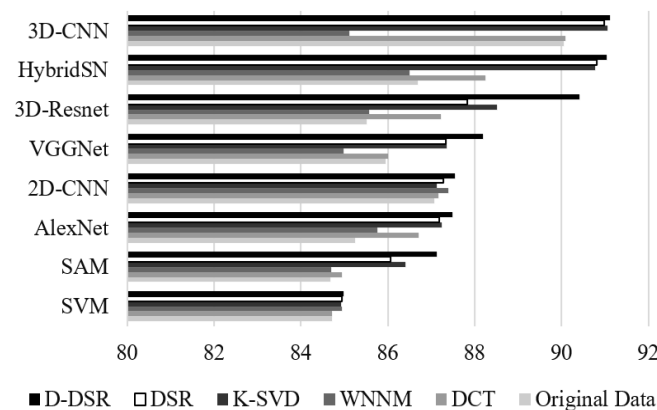


Fig. 16. AA values after classification of all considered methods at 20% training set (The six top-to-bottom enhancement methods in the same order as the labels from left to right).

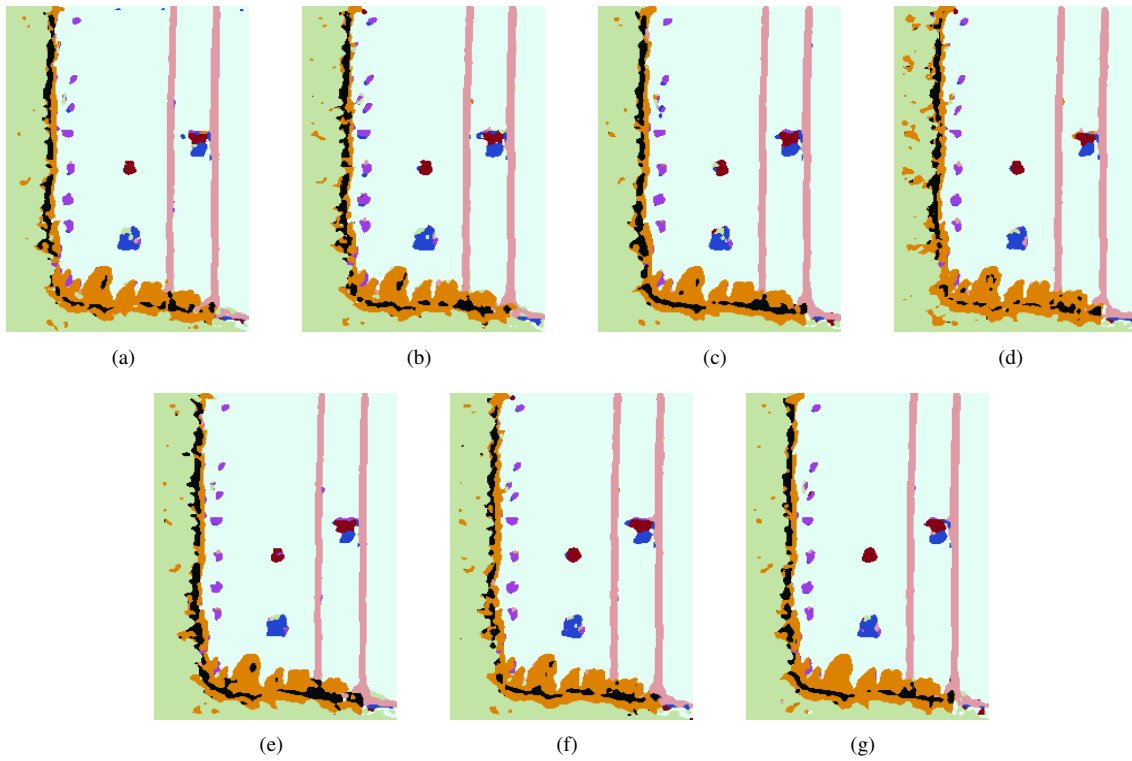


Fig. 17. Classification results of all data by SVM with 20% training data. Figure (a) is the classification result of the original data; Figures (b), (c), (d), (e) and (f) are the classification results after DCT, WNNM, K-SVD, DSR, and D-DSR enhancement respectively; Figure (g) is the classification result after DSR enhancement on spectral dimension.

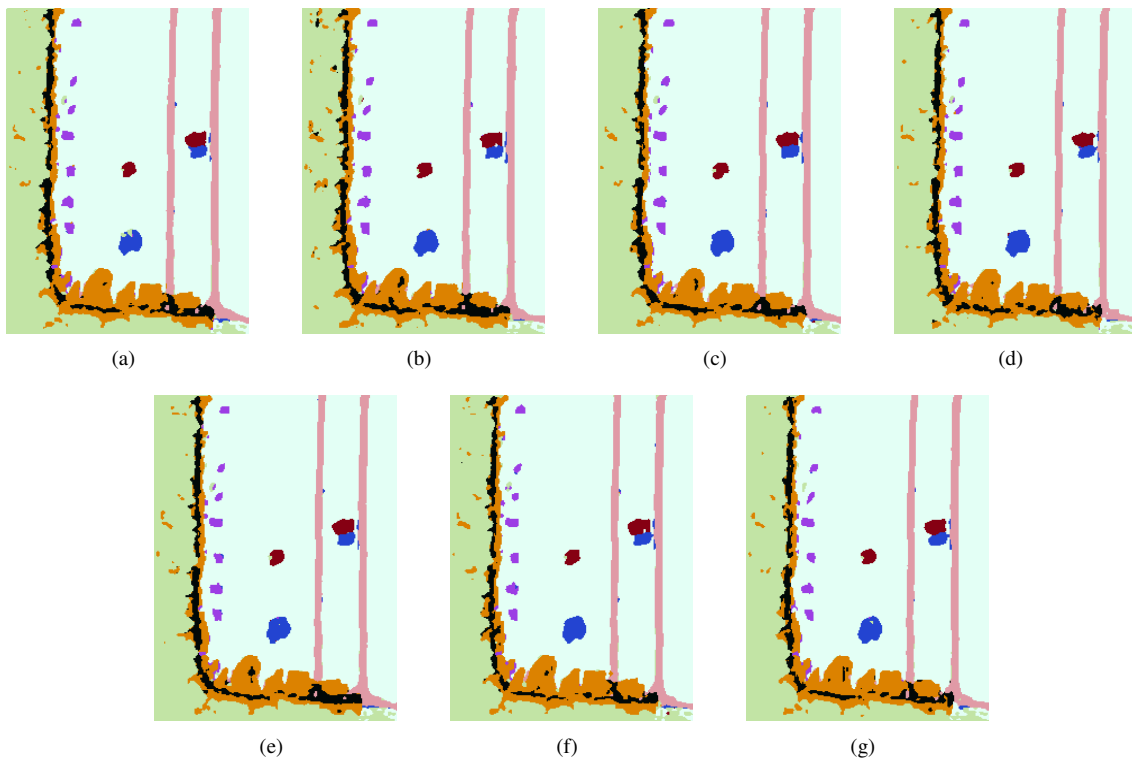


Fig. 18. Classification results of all data by SAM with 20% training data. Figure (a) is the classification result of the original data; Figures (b), (c), (d), (e) and (f) are the classification results after DCT, WNNM, K-SVD, DSR, and D-DSR enhancement respectively; Figure (g) is the classification result after DSR enhancement on spectral dimension.

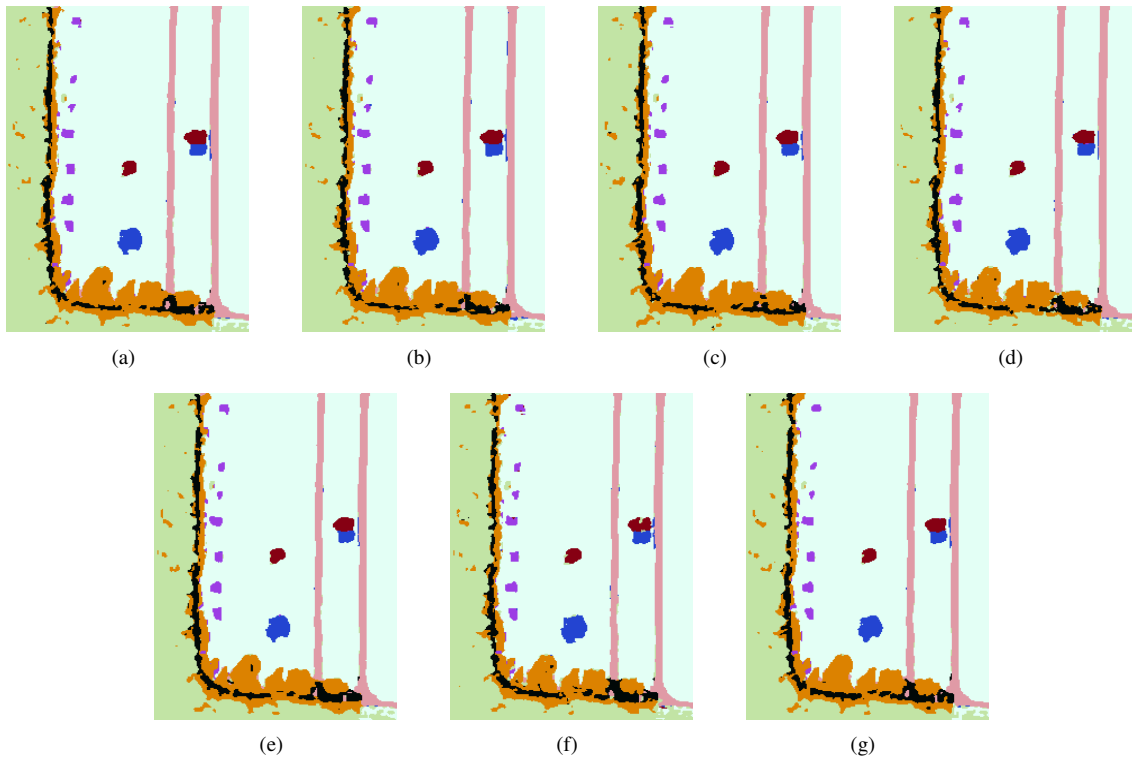


Fig. 19. Classification results of all data by AlexNet with 20% training data. Figure (a) is the classification result of the original data; Figures (b), (c), (d), (e) and (f) are the classification results after DCT, WNNM, K-SVD, DSR, and D-DSR enhancement respectively; Figure (g) is the classification result after DSR enhancement on spectral dimension.

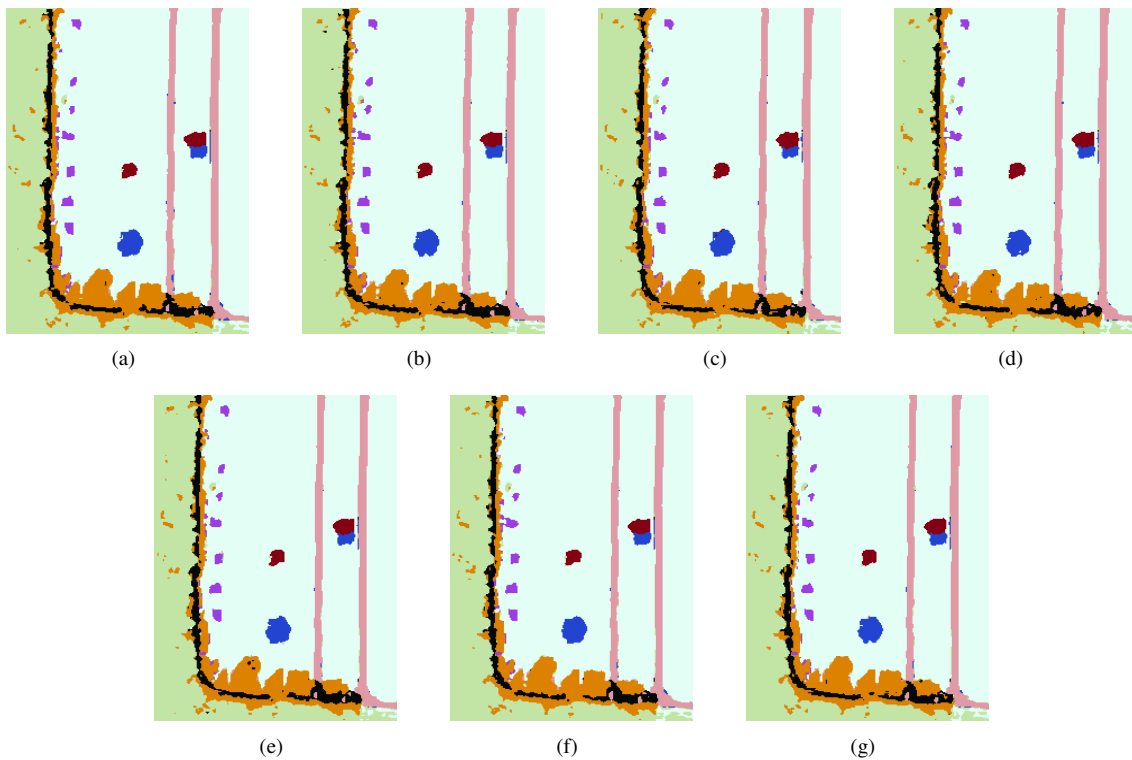


Fig. 20. Classification results of all data by 2D-CNN with 20% training data. Figure (a) is the classification result of the original data; Figures (b), (c), (d), (e) and (f) are the classification results after DCT, WNNM, K-SVD, DSR, and D-DSR enhancement respectively; Figure (g) is the classification result after DSR enhancement on spectral dimension.

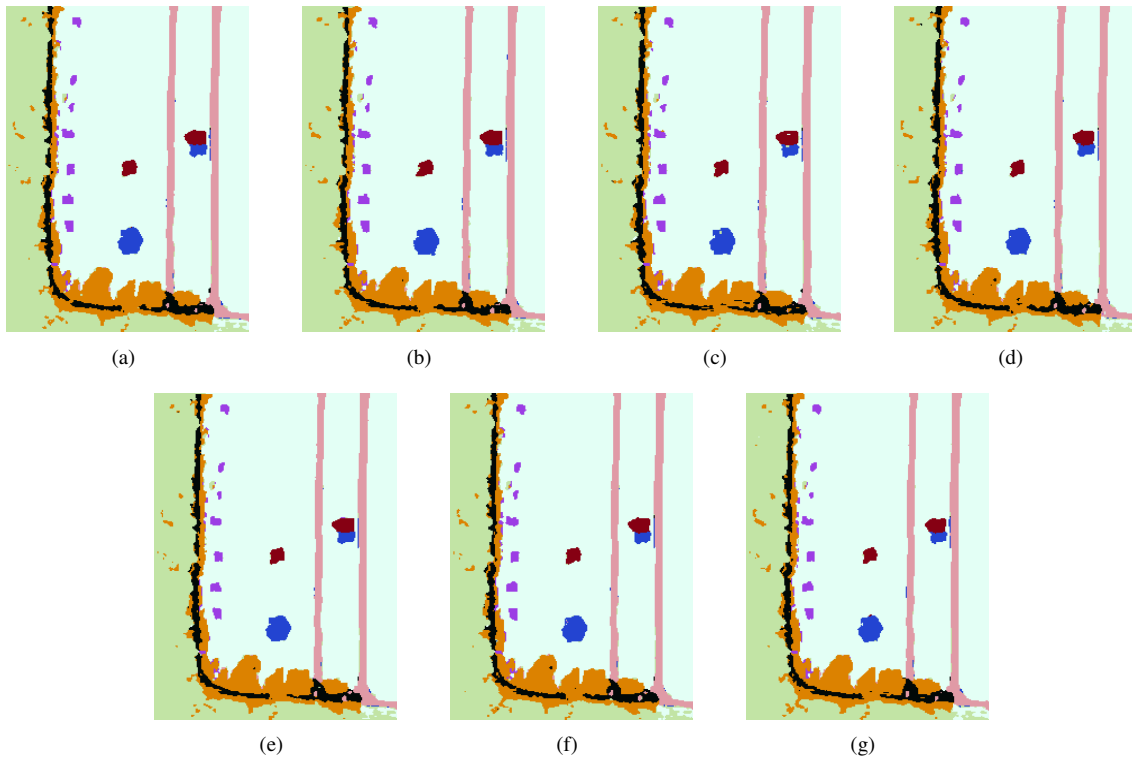


Fig. 21. Classification results of all data by VGGNet with 20% training data. Figure (a) is the classification result of the original data; Figures (b), (c), (d), (e) and (f) are the classification results after DCT, WNNM, K-SVD, DSR, and D-DSR enhancement respectively; Figure (g) is the classification result after DSR enhancement on spectral dimension.

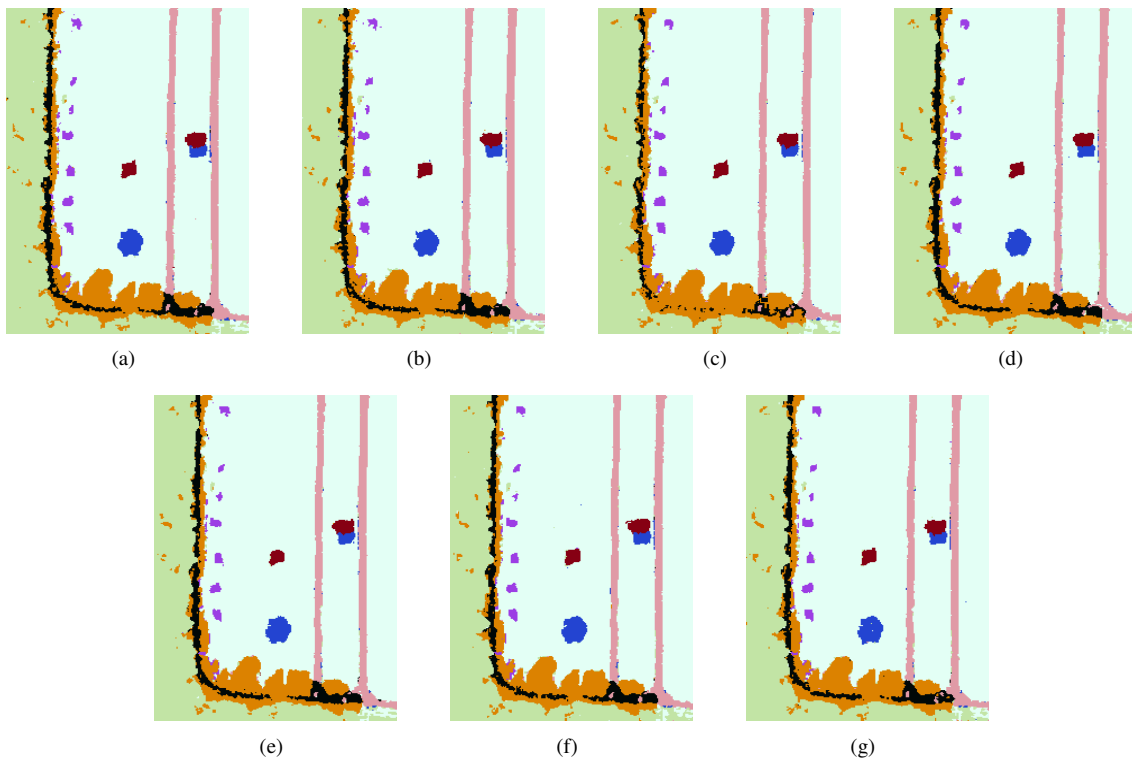


Fig. 22. Classification results of all data by 3D-ResNet with 20% training data. Figure (a) is the classification result of the original data; Figures (b), (c), (d), (e) and (f) are the classification results after DCT, WNNM, K-SVD, DSR, and D-DSR enhancement respectively; Figure (g) is the classification result after DSR enhancement on spectral dimension.

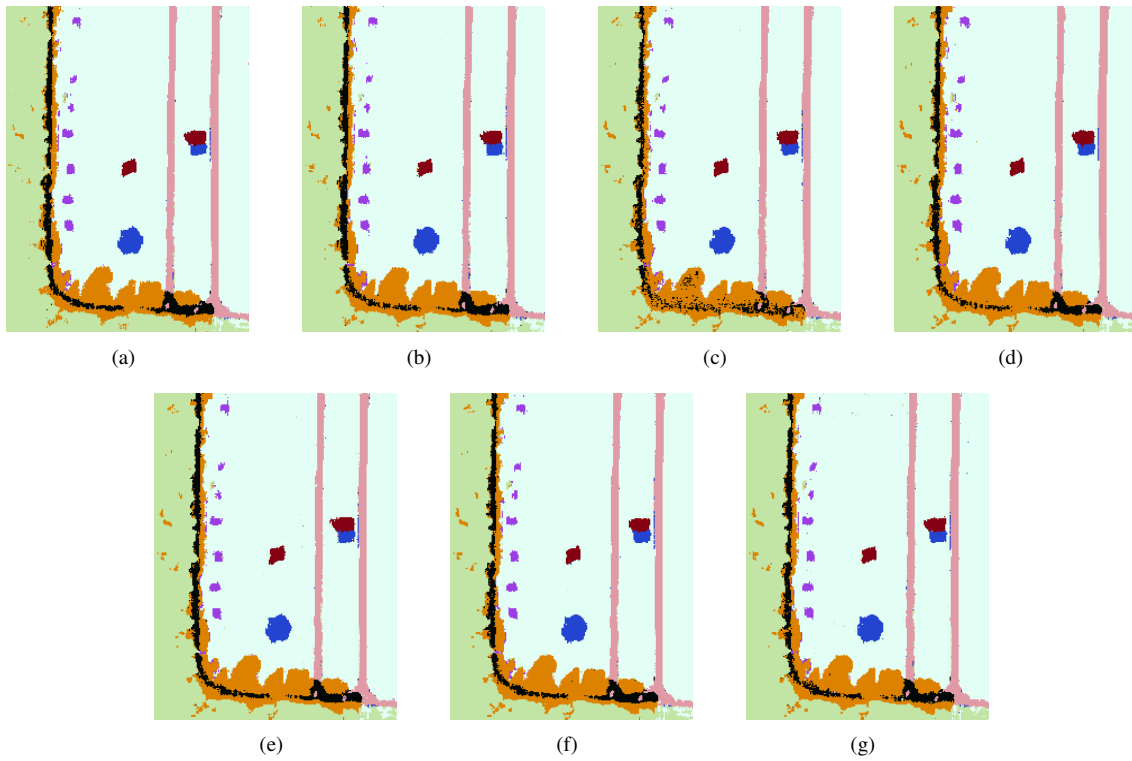


Fig. 23. Classification results of all data by HybridSN with 20% training data. Figure (a) is the classification result of the original data; Figures (b), (c), (d), (e) and (f) are the classification results after DCT, WNNM, K-SVD, DSR, and D-DSR enhancement respectively; Figure (g) is the classification result after DSR enhancement on spectral dimension.

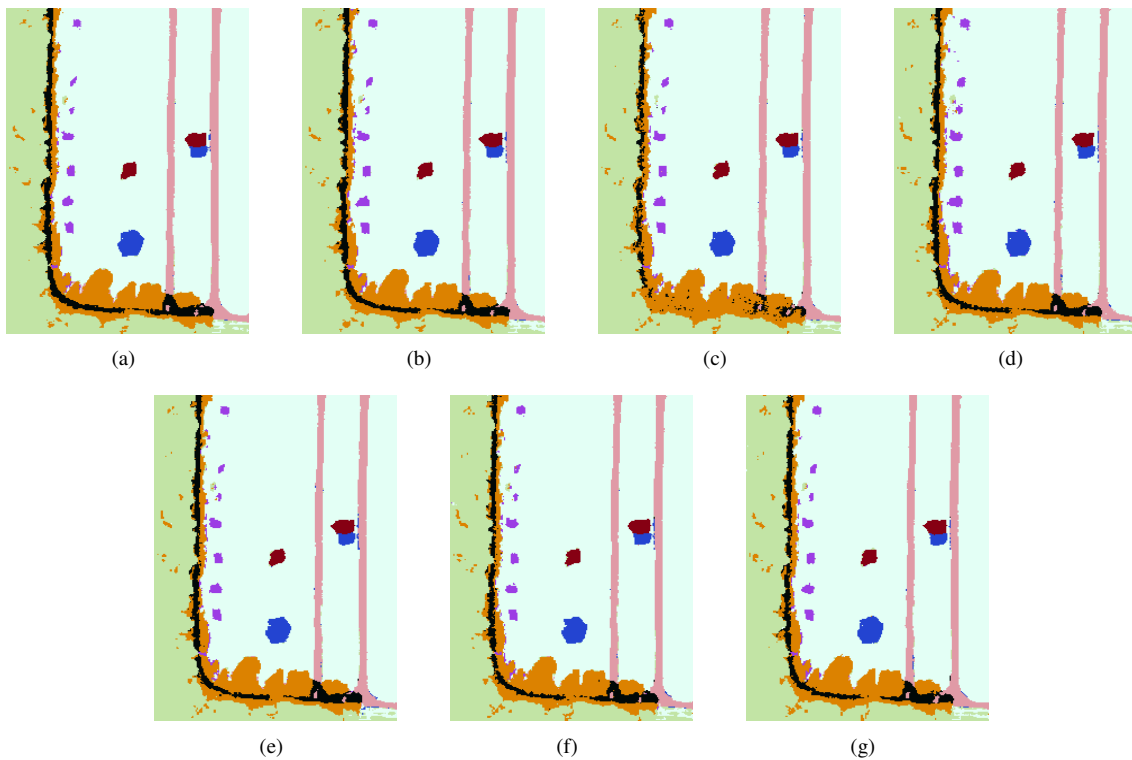


Fig. 24. Classification results of all data by 3D-CNN with 20% training data. Figure (a) is the classification result of the original data; Figures (b), (c), (d), (e) and (f) are the classification results after DCT, WNNM, K-SVD, DSR, and D-DSR enhancement respectively; Figure (g) is the classification result after DSR enhancement on spectral dimension.

- [3] P. Ghamisi, N. Yokoya, J. Li, W. Liao, S. Liu, J. Plaza, B. Rasti and A. Plaza, "Advances in Hyperspectral Image and Signal Processing: A Comprehensive Overview of the State of the Art," *IEEE Geoscience and Remote Sensing Magazine*, vol. 5, no. 4, pp. 37-78, 2017.
- [4] N. Kayet, K. Pathak and A. Chakrabarty, "Assessment of Foliar Dust Using Hyperion and Landsat Satellite Imagery for Mine Environmental Monitoring in an Open Cast Iron Ore Mining Areas," *Journal of Cleaner Production*, vol. 218, pp. 993-1006, 2019.
- [5] S. Meng, X. Wang, X. Hu, C. Luo and Y. Zhong, "Deep Learning-based Crop Mapping in the Cloudy Season Using One-shot Hyperspectral Satellite Imagery," *Computers and Electronics in Agriculture*, vol. 186, pp. 106188, 2021.
- [6] K. Slimani, Y. ruichek and R. messoussi, "Compound Facial Emotional Expression Recognition Using CNN Deep Features," *Engineering Letters*, vol. 30, no. 4, pp1402-1416, 2022.
- [7] X. Qiao, D. Yuan and H. Li, "Urban Shadow Detection and Classification Using Hyperspectral Image," *Journal of the Indian Society of Remote Sensing*, vol. 45, pp. 945-952, 2017.
- [8] L. Windrim, R. Ramakrishnan and A. Melkumyan, "A Physics-Based Deep Learning Approach to Shadow Invariant Representations of Hyperspectral Images," *IEEE Transactions on Image Processing*, vol. 27, no. 2, pp. 665-677, 2018.
- [9] A. Alzu'bi, A. Amira and N. Ramzan, "Learning Transfer Using Deep Convolutional Features for Remote Sensing Image Retrieval," *IAENG International Journal of Computer Science*, vol. 46, no. 4, pp637-644, 2019.
- [10] W. Sun, L. Tian, Y. Xu, B. Du and Q. Du, "A Randomized Subspace Learning Based Anomaly Detector for Hyperspectral Imagery," *Remote Sensing*, vol. 10, no. 3, pp. 417, 2018.
- [11] S. Bourennane, C. Fossati and A. Cailly, "Improvement of Classification for Hyperspectral Images Based on Tensor Modeling," *IEEE Geoscience and Remote Sensing Letters*, vol. 7, no. 4, pp. 801-805, 2010.
- [12] Y. Li, H. Zhang and Q. Shen, "Spectral-Spatial Classification of Hyperspectral Imagery with 3D Convolutional Neural Network," *Remote Sensing*, vol. 9, no. 1, pp. 67, 2017.
- [13] F. Xiong, J. Zhou and Y. Qian, "Material Based Object Tracking in Hyperspectral Videos," *IEEE Transactions on Image Processing*, vol. 29, pp. 3719-3733, 2020.
- [14] R. Benzi, A. Sutera and A. Vulpiani, "The Mechanism of Stochastic Resonance," *Journal of Physics A: Mathematical and General*, vol. 14, no. 11, pp. L453, 1981.
- [15] J. Liu, B. Hu and Y. G. Wang, "Optimum Adaptive Array Stochastic Resonance in Noisy Grayscale Image Restoration," *Physics Letters A*, vol. 383, no. 13, pp. 1457-1465, 2019.
- [16] R. Chouhan, R. K. Jha and P. K. Biswas, "Enhancement of Dark and Low-contrast Images Using Dynamic Stochastic Resonance," *IET Image Processing*, vol. 7, no. 2, pp. 174-184, 2013.
- [17] Q. Ye, H. Huang and C. Zhang, "Image Enhancement Using Stochastic Resonance Sonar Image Processing Applications," in *International Conference on Image Processing (ICIP) 2004*, pp. 263-266.
- [18] R. J. Marks, B. Thompson and M. A. El-Sharkawi, "Stochastic Resonance of a Threshold Detector: Image Visualization and Explanation," in *IEEE International Symposium on Circuits and Systems (ISCAS) 2002*, pp. IV-IV.
- [19] Y. Leng, Y. Guo and Y. Zhang, "Image Processing Based on Tuning-parameter Stochastic Resonance," in *ASME International Mechanical Engineering Congress and Exposition 2008*, pp. 873-877.
- [20] R. K. Jha, R. Chouhan, K. Aizawa and P. K. Biswas, "Dark and Low-contrast Image Enhancement Using Dynamic Stochastic Resonance in Discrete Cosine Transform Domain," *APSIPA Transactions on Signal and Information Processing*, vol. 2, 2013.
- [21] H. Bi, Y. Lei and Y. Han, "Stochastic Resonance Across Bifurcations in an Asymmetric System," *Physica A: Statistical Mechanics and its Applications*, vol. 525, pp. 1296-1312, 2019.
- [22] N. Gupta and R. K. Jha, "Enhancement of Dark Images Using Dynamic Stochastic Resonance with Anisotropic Diffusion," *IEEE Geoscience and Remote Sensing Letters*, vol. 25, no. 2, pp. 023017, 2016.
- [23] S. K. Swee, L. C. Chen, T. S. Chiang, and T. C. Khim, "Deep Convolutional Neural Network for SEM Image Noise Variance Classification," *Engineering Letters*, vol. 31, no. 1, pp328-337, 2023.
- [24] X. Glorot, A. Bordes and Y. Bengio, "Deep Sparse Rectifier Neural Networks," in *JMLR Workshop and Conference Proceedings 2011*, pp. 315-323.
- [25] Z. Zuo, B. Shuai, G. Wang, X. Liu, X. Wang, B. Wang and Y. Chen, "Learning Contextual Dependence with Convolutional Hierarchical Recurrent Neural Networks," *IEEE Transactions on Image Processing*, vol. 25, no. 7, pp. 2983-2996, 2016.
- [26] B. McNamara, K. Wiesenfeld and R. Roy, "Observation of Stochastic Resonance in a Ring Laser," *Physical Review Letters*, vol. 60, no. 25, pp. 2626, 1988.
- [27] M. I. Dykman, D. G. Luchinsky and R. Mannella, "Stochastic Resonance: Linear Response and Giant Nonlinearity," *Physical Review Letters*, vol. 70, no. 1, pp. 463-478, 1993.
- [28] N. Ahmed, T. Natarajan and K. R. Rao, "Discrete Cosine Transform," *IEEE Transactions on Computers*, vol. 100, no. 1, pp. 90-93, 1974.
- [29] S. Gu, L. Zhang, W. Zuo and X. Feng, "Weighted Nuclear Norm Minimization with Application to Image Denoising," in *IEEE Conference on Computer Vision and Pattern Recognition 2014*, pp. 2862-2869.
- [30] M. Aharon, M. Elad and A. Bruckstein, "K-SVD: An Algorithm for Designing Overcomplete Dictionaries for Sparse Representation," *IEEE Transactions on Signal Processing*, vol. 54, no. 11, pp. 4311-4322, 2006.
- [31] K. Makantasis, K. Karantzalos, A. Doulamis and N. Doulamis, "Deep Supervised Learning for Hyperspectral Data Classification Through Convolutional Neural Networks," in *IEEE International Geoscience and Remote Sensing Symposium 2015*, pp. 4959-4962.
- [32] S. K. Roy, G. Krishna, S. R. Dubey and B. B. Chaudhuri, "HybridSN: Exploring 3-D-2-D CNN Feature Hierarchy for Hyperspectral Image Classification," *IEEE Geoscience and Remote Sensing Letters*, vol. 17, no. 2, pp. 277-281, 2019.
- [33] Y. Bengio, "Lecture Notes in Computer Science," *IEEE Geoscience and Remote Sensing Letters*, vol. 7700, pp. 277-281, 2012.
- [34] X. Liu, Q. Sun, Y. Meng, M. Fu and S. Bourennane, "Hyperspectral Image Classification Based on Parameter-Optimized 3D-CNNs Combined with Transfer Learning and Virtual Samples," *Remote Sensing*, vol. 10, no. 9, pp. 1425, 2018.
- [35] N. Renard and S. Bourennane, "Improvement of Target Detection Methods by Multiway Filtering," *IEEE Transactions on Geoscience and Remote Sensing*, vol. 46, no. 8, pp. 2407-2417, 2008.
- [36] X. Liu, S. Sun and M. Fu, "HSI Classification Based on Multimodal CNN and Shadow Enhance by DSR Spatial-Spectral Fusion," *Canadian Journal of Remote Sensing*, vol. 47, no. 6, pp. 773-789, 2021.
- [37] A. Sellami, M. Farah and I. R. Farah, "Hyperspectral Imagery Classification Based on Semi-supervised 3-D Deep Neural Network and Adaptive Band Selection," *Expert Systems with Applications*, vol. 129, pp. 246-259, 2019.

Yang. yang Kou is a postgraduate student of Control Science and Engineering in the School of Automation and Electronic Engineering, Qingdao University of Science and Technology. She has studied hyperspectral image processing algorithms based on dynamic stochastic resonance during her postgraduate study. She has mastered the establishment and implementation of hyperspectral image enhancement algorithms, Python programming, and some models of deep learning algorithms for image classification.

Xue. feng Liu is a professor, master's supervisor and doctoral supervisor in the School of Automation and Electronic Engineering, Qingdao University of Science and Technology. She received her PhD in Optics, Photonics and Image Processing from the Université Centrale de Marseille, France. Published more than 30 academic papers in important journals or international conferences at home and abroad, including nearly 10 SCI-indexed papers and more than 20 EI-indexed papers. Presided over the National Natural Science Foundation of China (NSFC), the Natural Science Foundation of Shandong Province (NSFC) and the Research Start-up Fund for Returnees to China, Ministry of Education. Participated in the project of the National Natural Science Foundation of China, the project of the Ministry of Construction of China, the project of Shandong Province Science and Technology Tackle, etc. Won the third prize of Shandong Higher Education Science and Technology Award. Instructed master's students to obtain: one excellent master's thesis in Shandong Province and three excellent master's theses at university level.